Accepted Manuscript

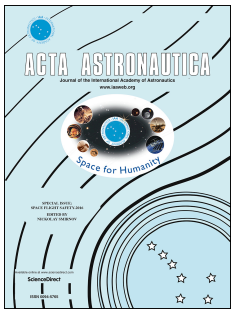

Systematic performance-oriented guidance tuning for descent & landing on small planetary bodies

Pedro Simplício, Andrés Marcos, Eric Joffre, Mattia Zamaro, Nuno Silva

PII: S0094-5765(17)31883-0

DOI: 10.1016/j.actaastro.2018.07.028

Reference: AA 7009

To appear in: *Acta Astronautica*

Received Date: 21 December 2017

Accepted Date: 14 July 2018

Please cite this article as: P. Simplício, André. Marcos, E. Joffre, M. Zamaro, N. Silva, Systematic performance-oriented guidance tuning for descent & landing on small planetary bodies, *Acta Astronautica* (2018), doi: 10.1016/j.actaastro.2018.07.028.

Systematic Performance-oriented Guidance Tuning for Descent & Landing on Small Planetary Bodies☆

Pedro Simplício[a,*], Andrés Marcos[a], Eric Joffre[b], Mattia Zamaro[b], Nuno Silva[b]

[a] *University of Bristol, Queen's Building, University Walk, Bristol BS8 1TR, UK*
[b] *Airbus Defence and Space Ltd, Gunnels Wood Road, Stevenage SG1 2AS, UK*

Abstract

Descent & landing (D&L) on small planetary bodies are scientifically rewarding exploration missions but they are technically challenging due to the complex and poorly-known environment around those bodies. The standard guidance synthesis approach considers nominal conditions and applies optimal control theory to obtain guidance law gains, followed by intensive verification and validation. In this article, it is shown that the standard approach may yield gains that are not optimal once dispersions (and/or other optimality metrics) are taken into account and a tuning approach is then proposed based on *a priori* methodological system assessment. The proposed approach employs systematic high-fidelity simulations to generate trade-off maps. These maps can be generated by on ground operators based on the best estimated conditions and uploaded to the spacecraft as it approaches the target. The proposed systematic guidance tuning and resulting maps also provide a valuable understanding of the system dynamics towards the application of other industry-oriented tools such as structured $\mathcal{H}_\infty$ optimisation. It is shown that the proposed tuning enables propellant consumption reductions of around 40% compared to state-of-practice gain selections.

Keywords: Descent & landing, Optimal guidance, Structured $\mathcal{H}_\infty$ control

☆This work is funded by the UK Space Agency through a 2016 NSTP-2 Space Technology Fast Track grant entitled "Robust and Nonlinear Guidance and Control for Landing on Small Bodies". Mr. Simplício is also the recipient of a Doctoral Training Partnership award by the UK Engineering and Physical Sciences Research Council.

*Corresponding author
Email address: pedro.simplicio@bristol.ac.uk (Pedro Simplício)
URL: www.tasc-group.com (Technology for AeroSpace Control Group)

1. Introduction

A renewed scientific interest has been growing in the exploration of small asteroids in addition to larger planetary bodies such as Mars, since their weaker gravitational field makes them more easily accessible. However, these exploration missions are very challenging from an engineering perspective, particularly if the natural dynamics in the vicinity of the target asteroid is exploited to alleviate descent & landing (D&L) propellant consumption requirements. This is because small planetary bodies are typically characterised by highly irregular and poorly-known shapes, which render their physical environment extremely uncertain and variable. Moreover, due to the interplanetary distances involved, fully autonomous guidance algorithms are required to cope with communication delays and spacecraft subsystems degradation, as demonstrated by the European Rosetta mission (Falcoz et al., 2015). For all the above reasons, the Space community has recognised the need for robust D&L architectures.

As part of the UK Space Agency's National Space Technology Programme, the University of Bristol and Airbus Defence and Space were awarded the project entitled "Robust and Nonlinear Guidance and Control for Landing on Small Bodies", with the aim to investigate the application of advanced robust techniques for the design and optimisation of D&L approaches. Although a generic framework was pursued, the project focused on the Martian moon Phobos, which is among ESA's candidates for an interplanetary sample return (SR) mission due to the scientific interest on its formation, as well as a technological precursor for the exploration of the Martian System (Barraclough et al., 2014).

In fact, a renewed interest in small planetary bodies has led to several studies and missions in recent years. There are mainly two different purposes behind these studies and missions. On the one hand, there is the exploitation of hypervelocity impact with a spacecraft as a mitigation strategy against objects on a course for potential collision with Earth. Notable examples of this type of missions include NASA's Deep Impact Spacecraft (Kubitschek, 2003), which

successfully hit comet Tempel 1 on July 2005 at 10 km/s, while ESA's Asteroid Impact Mission (Ferrari et al., 2015), undergoing preliminary design phase but planned to rendezvous with the Didymos binary asteroid system (and observe closely the collision with an impactor a few months after).

On the other hand, there is also the interest of touch-and-go or landing on planetary bodies instead of impacting, as the scientific return in general is much higher. Successful missions in this category include NASA's Stardust (Bhaskaran et al., 2004), the first SR mission, launched in 1999 to collect comet and cosmic dust samples, JAXA's Hayabusa (Yoshimitsu et al., 2009), a mission that landed on Itokawa asteroid on November 2005 returning to Earth five years after, and ESA's Rosetta (Geurts et al., 2014), which performed a rendezvous with comet Churyumov-Gerasimenko and delivered a lander for on-site analysis on November 2014. In addition, NASA has launched OSIRIS-REx (Lauretta & OSIRIS-REx Team, 2012) on September 2016, an SR spacecraft that will reach the near-Earth asteroid Bennu.

In all these applications, a successful guidance technique is translated into an acceptable *trade-off* between allowable position and velocity errors versus propellant consumption or ΔV needed for the manoeuvre. The earliest known algorithm is inspired by the missile interception problem. It is known as proportional navigation guidance (PNG) and introduced in (Zarchan, 1994), where a method of augmenting it when the target acceleration is known or can be assumed is also provided. In addition, guidance using predictive manoeuvres based on linear orbital perturbation theory (Battin, 1987) is proven possible and complemented with PNG in (Gil-Fernandez et al., 2008). However, most of the work on closed-loop feedback guidance for small bodies recasts the problem as optimal feedback control with terminal constraints, for which optimal conditions can be analytically derived using the Pontryagin maximum principle (Battin, 1987) or through calculus of variations (D'Souza, 1997).

This type of laws has been continuously developed for different terminal boundary conditions (e.g., constrained velocity, free velocity, constrained intercept-angle, etc.) and also related to the classical PNG laws (see, for exam-

ple, (Guo et al., 2011; Hawkins et al., 2012)). Nevertheless, the aforementioned optimal conditions are only practical under the assumption of simplified and *well-known* gravitational fields.

From the surveyed techniques, a reconciliation, in exactitude an underlying parametric generalisation, of D&L laws was identified (Simplício et al., 2017). Although this parametrisation seems to be a simple step, it enabled to identify the possibility of applying systematic tuning methodologies, which may prove to be a paradigm change in the current state-of-practice for D&L guidance and control on small bodies.

In this paper, a systematic tuning methodology that relies on the identified parametric generalisation is presented and applied to Phobos D&L guidance tuning. This approach employs a methodological evaluation of a high-fidelity model (see Sec. 2) over the parameter space to generate *trade-off maps* that enable a clear performance quantification of candidate guidance solutions. In addition, this approach provides a valuable understanding of the system dynamics that supports the application of other tools addressed in the project, including structured $\mathcal{H}_\infty$ optimisation (Gahinet & Apkarian, 2011; Apkarian et al., 2015). This tool has been successfully employed to design control compensators that effectively enable the use of simpler guidance schemes (Simplício et al., 2018).

With this in mind, the paper begins in Sec. 2 with an introduction of the D&L problem and benchmark, followed by the description and application of the tuning methodology using systematic simulation in Sec. 3 and by its reconciliation with structured $\mathcal{H}_\infty$ optimisation in Sec. 4.

2. D&L Problem and benchmark

The generic planetary D&L problem configuration is depicted in Fig. 1 for planar motion but without loss of generality. It describes a spacecraft approaching a moving body target subject to the influence of a larger one. Here, the X and Y axes arbitrarily define an inertial reference frame with origin at the centre of the larger body. For this problem, it is assumed that the spacecraft has a

dedicated attitude control system that maintains a nadir pointing during the descent (actually a requirement of visual-navigation systems). Couplings are then considered at actuator level by reserving a fraction of the available thruster authority (10 to 20%) for attitude control.

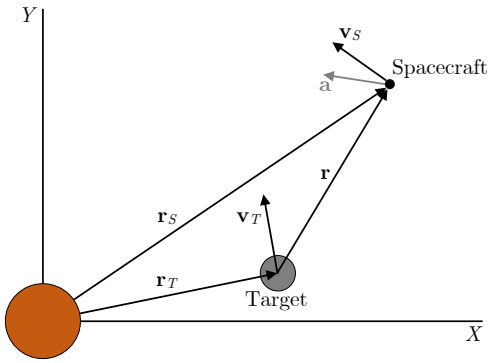

Figure 1: Problem geometry

Based on this figure, the D&L problem lies on the computation of the acceleration input $\mathbf{a}(t)$ between initial and final times, i.e., $t = t_0$ and $t = t_f$, that must be able to:

- Bring the relative position and velocity from the initial boundary conditions $\mathbf{r}(t_0) = \mathbf{r}_0$ and $\mathbf{v}(t_0) = \mathbf{v}_0$ to the final conditions $\mathbf{r}(t_f) = \mathbf{r}_f$ and $\mathbf{v}(t_f) = \mathbf{v}_f$;
- Cope with the effect of uncertainties (mostly related to an inexact gravitational model) and perturbations (such as thruster realisation errors and inaccurate sensor measurements).

In this problem, the duration from a given instant of time t until the end of the manoeuvre is known as time-to-go, $t_{\text{go}}(t) = t_f - t$, the norm of the relative vector between spacecraft $\mathbf{v}_S(t)$ and target velocities $\mathbf{v}_T(t)$ is known as closing speed and is given by $V_c(t) = ||\mathbf{v}_S(t) - \mathbf{v}_T(t)||$ and finally the unit vector from target to spacecraft is known as line-of-sight $\mathbf{\Lambda}(t) = \mathbf{r}(t)/||\mathbf{r}(t)||$. In addition, and specially important to reconcile the guidance laws addressed in this paper, the concept of zero-effort errors (Ebrahimi et al., 2008) must be introduced:

- Zero-effort-miss (ZEM) is the position error at the end-of-mission if no manoeuvres are made after time t:

$$\mathbf{ZEM}(t) = \mathbf{r}_f - \mathbf{r}(t_f) \mid \mathbf{a}(\tau) = 0 \; \forall \; \tau \in [t, t_f] \tag{1}$$

- Zero-effort-velocity (ZEV) is the velocity error at the end-of-mission if no manoeuvres are made after time t:

$$\mathbf{ZEV}(t) = \mathbf{v}_f - \mathbf{v}(t_f) \mid \mathbf{a}(\tau) = 0 \; \forall \; \tau \in [t, t_f] \tag{2}$$

To obtain analytical expressions for ZEM and ZEV, the apparent gravity is typically assumed to be known as an explicit function of time. However, as gravity is more generally given as a function of position, the computation of ZEM and ZEV is approximated or performed numerically (Hawkins et al., 2012).

2.1. High-fidelity dynamics in the vicinity of Phobos

Landing on Phobos is particularly challenging because of its reduced mass (it is 8 orders of magnitude smaller than Mars) and proximity to the red planet (mean orbital altitude about 6000 km), which causes the planet's sphere of influence to end just 3.5 km above Phobos' surface (Fig. 2a). Hence, there is no possibility for Keplerian orbits around Phobos and the third-body perturbation of Mars cannot be neglected.

Furthermore, due to the irregular shape and mass distribution of Phobos, the gravity of the moon cannot be accurately accounted for by a spherical field, and requires to be described using a gravity harmonics (GH) model (Fig. 2b). In this case, using spherical coordinates (r, θ, ϕ) for distance to barycentre, co-latitude and longitude, as well as R for a reference radius and μ_{g} for the gravitational constant, the gravity potential is given by:

$$U_{\mathrm{g}}(r, \theta, \phi) = \frac{\mu_{\mathrm{g}}}{R} \sum_{n=0}^{\bar{n}} \left(\frac{R}{r} \right)^{n+1} \sum_{m=0}^{n} C_n^m(\phi) P_n^m(\cos\theta) \tag{3}$$

where $P_n^m(x)$ are the associated Legendre polynomials and:

$$C_n^m(\phi) = C_{n,m} \cos m\phi + S_{n,m} \sin m\phi \tag{4}$$

is the expansion of the GH coefficients $C_{n,m}$ and $S_{n,m}$. For Phobos, $\bar{n} = 4$ (i.e., 28 coefficients) is assumed to suffice.

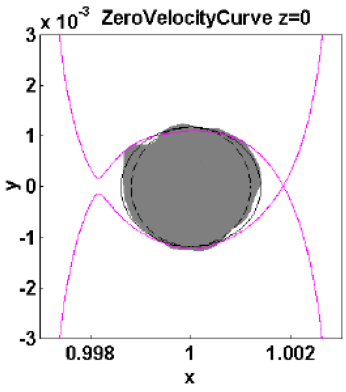

(a) Mars' sphere of influence around Phobos. Axes normalised by mean distance Mars-Phobos. Continuous black line represents Phobos ellipsoid and dashed line its mean sphere.

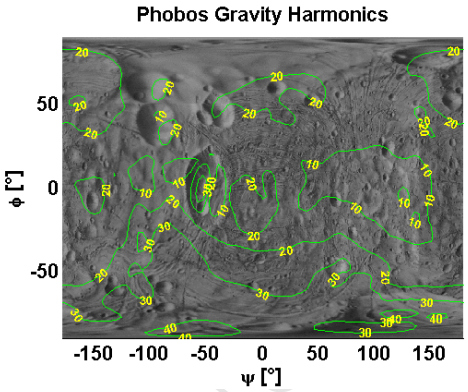

(b) Percentage difference of gravitational acceleration between gravity harmonics and Keplerian model at Phobos' surface.

Figure 2: Highly inhomogeneous gravitational field of Phobos [Credits: Airbus Defence and Space]

Estimates of Phobos' GH coefficients are available from on-ground observations but, due to its complex gravitational environment and distance to Earth, 19 of them are known with a large range of uncertainty. In this work, each coefficient is assumed to follow a Gaussian distribution with standard deviation equal to its nominal value. Further details on this assumption and on the nominal GH coefficients are provided in (Zamaro & Biggs, 2015; Joffre et al., 2017).

It is therefore mandatory that every candidate guidance algorithm is verified not only for nominal GH coefficients, but also for all admissible values within the uncertainty range. In practice, this range may be significantly reduced before D&L if an observation phase of the target body is included in the mission. The possibility of guidance retuning upon the availability of updated estimates is actually an added-value of the proposed methodology, as discussed in Sec. 3.2.

Given the small eccentricity of Phobos' orbit around Mars (approximately 0.015), the nonlinear dynamics of a spacecraft in the vicinity of Mars-Phobos system is typically described as a circular restricted three-body problem. In this case, its motion can be written in a body-centred body-fixed (BCBF) frame with origin at the moon's barycentre as:

$$\begin{bmatrix}\dot{\mathbf{r}}(t) & \dot{\mathbf{v}}(t) & \dot{\nu}(t)\end{bmatrix}^{\mathrm{T}} = \mathbf{f}\left(\mathbf{r}(t), \mathbf{v}(t), \nu(t)\right) + \begin{bmatrix}0_{3\times3} & I_{3\times3} & 0_{1\times3}\end{bmatrix}^{\mathrm{T}} \mathbf{a}(t) \quad (5)$$

where the state vector $\begin{bmatrix}\mathbf{r}(t) & \mathbf{v}(t) & \nu(t)\end{bmatrix}^{\mathrm{T}}$ gathers the position and velocity of the spacecraft with respect to Phobos, as well as the true anomaly of the latter around Mars, while the control vector $\mathbf{a}(t)$ represents any propulsive acceleration generated by the spacecraft in the BCBF frame. The effects of the complex and uncertain gravity field enter in $\mathbf{f}\left(\mathbf{r}(t), \mathbf{v}(t), \nu(t)\right)$ through the dynamics of $\mathbf{v}$, which are given (dropping now the dependence on t for clarity) as:

$$\dot{\mathbf{v}} = \boldsymbol{\nabla} U_{\mathrm{SC}}^{\mathrm{Pho}}(\mathbf{r}) + \boldsymbol{\nabla} U_{\mathrm{SC}}^{\mathrm{Mars}}(\mathbf{r}, \nu) - \boldsymbol{\nabla} U_{\mathrm{Pho}}^{\mathrm{Mars}}(\nu) - \omega_{\mathrm{Pho}} \times (\omega_{\mathrm{Pho}} \times \mathbf{r}) - 2\omega_{\mathrm{Pho}} \times \mathbf{v} \quad (6)$$

In this equation, the first three terms represent respectively the gravity of Phobos on the spacecraft, Mars on the spacecraft and Mars on Phobos, computed as a function of the position $\mathbf{r}$ of the spacecraft relative to Phobos and of the latter's location around Mars (via its true anomaly ν). These calculations rely on the gravity potential description of Eq. (3) and become particularly complex due to the frame transformations involved, see (Zamaro & Biggs, 2015). The remaining terms account for the non-inertial acceleration caused by the fact that the BCBF frame is rotating with Phobos at a rate ω_{Pho}.

2.2. Candidate guidance architectures

With the "spacecraft dynamics & kinematics" (SDK) defined as in Sec. 2.1, the high-fidelity simulator depicted in Fig. 3 has been developed by Airbus based on their Space operational experience.

In order to accurately model the D&L spacecraft behaviour, as depicted in the figure, the SDK computation is preceded by an "allocation & actuation" block, accounting for thruster realisation errors (e.g., mounting misalignments and

limited control authority) and is followed by a "sensors & navigation" module, which implements the algorithms executed to produce relative position and velocity estimates, $\hat{\mathbf{r}}(t)$ and $\hat{\mathbf{v}}(t)$. Environment effects are included in the SDK block. Actuation errors are time and trajectory dependent, but bounded in the order of 0.15 m/s^2. Navigation algorithms introduce two different perturbations: a quantisation error (due to the fact that $\hat{\mathbf{r}}(t)$ and $\hat{\mathbf{v}}(t)$ are updated every 60 seconds) and coloured noise.

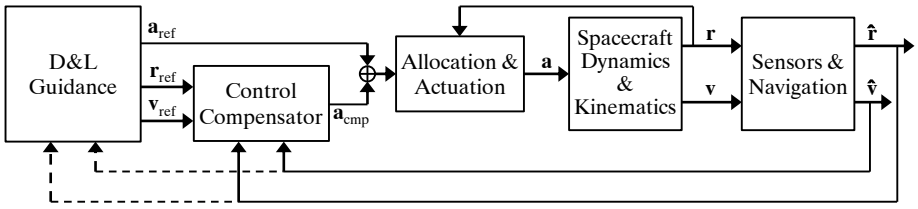

Figure 3: Benchmark architecture (- - - - indicates information flow for closed-loop guidance)

These blocks are part of Airbus' industrial testing, simulation & assessment (TSA) facility and will be employed for system development and verification in case of a future Phobos SR mission. In addition, the "D&L guidance" logic is included as required. Two different guidance paradigms are defined: open-loop and closed-loop. These paradigms are detailed in Sec. 2.2.1 and 2.2.2.

Finally, to further alleviate trajectory errors, the architecture of Fig. 3 is optionally augmented with a "control compensator", which introduces an additional acceleration vector command $\mathbf{a}_{\text{cmp}}(t)$ that compensates for deviations between reference and measured position and velocity. The focus of this paper, however, is not on this compensator and hence its action is not considered for guidance tuning. In fact, in the ideal case, this module has no effect on the system since there are no deviations. For further details on this type of compensation, the reader is referred to (Simplício et al., 2018).

2.2.1. Open-loop guidance

Open-loop (or implicit) guidance is employed when a reference trajectory $\{\mathbf{r}_{\text{ref}}(t), \mathbf{v}_{\text{ref}}(t)\}$ and thruster profile $\mathbf{a}_{\text{ref}}(t)$ are generated before, and remain

unchanged during, the descent. In the case of Phobos, with a complex and poorly-know gravitational field, this approach has been shown not to be robust enough for a successful D&L landing strategy (Joffre et al., 2017).

For this study, reference trajectories (RTs) were designed through the following process: [i] analysis of a set of unstable manifolds originated at Libration Point Orbits (LPOs) in the three-body system that intersect Phobos (Fig. 4a), [ii] selection of the manifolds the reach the moon with higher incidence angle and lower closing speed as initial guesses, [iii] definition of a polynomial acceleration profile aimed at bringing the final closing speed to zero and [iv] optimisation of the initial guesses and acceleration profile via nonlinear programming, with the objective of minimum propellant consumption or ΔV, given as:

$$\Delta V(t) = \int_0^t \left[\mathbf{a}^{\mathrm{T}}(\tau)\,\mathbf{a}(\tau)\right]^{1/2} \mathrm{d}\tau \tag{7}$$

For a detailed description on this process, the reader is referred to (Joffre et al., 2017). The three trajectories visible in Fig. 4b will be addressed in this paper, with a stronger emphasis on RT1 to illustrate the proposed tuning methodology.

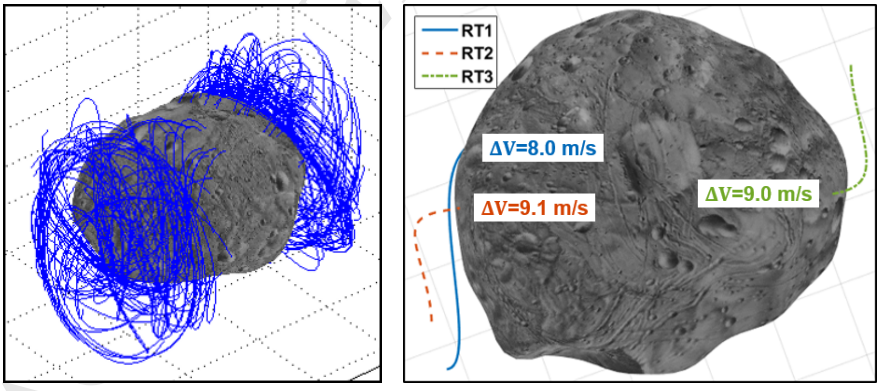

(a) Candidate manifolds (b) Optimised trajectories and total ΔV

Figure 4: Reference D&L trajectory design

2.2.2. Closed-loop guidance

Closed-loop (or explicit) guidance refers to the case when the thruster profile is computed in real-time to correct the trajectory based on onboard measurements, as shown in Fig. 3 by the dashed lines. In this case, the "D&L guidance" subsystem is also responsible for the computation of auxiliary variables such as line-of-sight or zero-effort errors.

As mentioned before, although distinct types of closed-loop laws have been identified, they share structural commonalities and can be generalised using line-of-sight or zero-effort error kinematics (Simplício et al., 2017) as follows:

$$\mathbf{a}(t) = \begin{bmatrix} k_r & k_v \end{bmatrix} V_c(t) \begin{bmatrix} \dfrac{\mathbf{\Lambda}(t)}{t_{\mathrm{go}}(t)} \\ \\ \dot{\mathbf{\Lambda}}(t) \end{bmatrix} - \phi\, \mathbf{h}\left(\mathbf{\Lambda}(t), \dot{\mathbf{\Lambda}}(t), t_{\mathrm{go}}(t)\right) \tag{8}$$

$$\mathbf{a}(t) = \begin{bmatrix} k_r & k_v \end{bmatrix} \begin{bmatrix} \dfrac{\mathbf{ZEM}(t)}{t_{\mathrm{go}}^2(t)} \\ \\ \dfrac{\mathbf{ZEV}(t)}{t_{\mathrm{go}}(t)} \end{bmatrix} - \phi\, \mathbf{h}\left(\mathbf{ZEM}(t), \mathbf{ZEV}(t), t_{\mathrm{go}}(t)\right) \tag{9}$$

These equations show a fixed structure formed by a linear component, parameterised through gains k_r and k_v, plus a nonlinear function $\mathbf{h}(\cdot)$ weighted by the constant ϕ, which can be introduced to improve robustness properties but will be set to zero from now on for simplicity. Line-of-sight and zero-effort errors can be defined directly with respect to the landing site or, also for improved robustness, to a set of intermediate waypoints. For this study, the latter option is adopted, using waypoints from the reference trajectories of Fig. 4b.

Depending on the choice of gains $\{k_r,\, k_v\}$, closed-loop guidance laws may present very different properties. For the case of constrained terminal velocity guidance (CTVG), standard values of {6, -2} for the gains in Eq. (9) can be analytically derived (Guo et al., 2011; Hawkins et al., 2012) by recasting the D&L problem as an optimal control with constrained terminal position and

velocity and using the cost function:

$$J(\mathbf{a}(t)) = \frac{1}{2}\int_0^{t_f} \mathbf{a}^{\mathrm{T}}(\tau)\,\mathbf{a}(\tau)\,\mathrm{d}\tau \tag{10}$$

Note that this problem does not represent a direct minimisation of ΔV in Eq. (7), but it is generally easier to solve and provides a representative solution. Furthermore, the derivation is carried out under the assumption of simplified and well-known gravitational fields, which does not hold for the case of Phobos.

The aim of this paper is therefore to revisit and try to improve the standard gain selection for complex and perturbed gravitational environments such as Phobos.

3. Guidance tuning via systematic simulation

This section presents the closed-loop guidance tuning methodology developed via systematic simulation. It starts (Sec. 3.1) with a thorough exposition of the proposed approach and with the results obtained for RT1, followed in Sec. 3.2 by its application to the other two trajectories (recall Fig. 2b). The section concludes with a Monte-Carlo (MC) validation campaign in Sec. 3.3.

3.1. Proposed approach

A successful guidance tuning is always a translation of an appropriate trade-off between acceptable touchdown (position and velocity) accuracy and the total ΔV needed for the D&L manoeuvre. As mentioned before, using results from optimal control theory, standard closed-loop guidance gains can be analytically derived. Nevertheless, these gains are only practical under the assumption of simplified and well-known gravitational fields.

In order to provide not just a systematic tuning methodology in the case of highly complex and perturbed gravitational environments, but also a clear understanding of the aforementioned trade-off, a simulation-based approach is proposed in this paper. This approach relies on the availability of a nonlinear high-fidelity simulation model (in the present case the model introduced in Sec. 2.2) to evaluate three key performance indicators:

- R_c - Target distance (position error) at touchdown, i.e. $||\mathbf{r}_f - \mathbf{r}(t_f)||$;
- V_c - Closing speed (velocity error) at touchdown, i.e. $||\mathbf{v}_f - \mathbf{v}(t_f)||$;
- ΔV - Total ΔV, given by Eq. (7) with $t = t_f$.

Also as introduced in Sec. 2.2, the proposed tuning approach is illustrated using the parametric guidance generalisation of Eq. (9) and a set of intermediate waypoints from trajectory RT1. This approach is described in the following paragraphs.

3.1.1. Nominal indicators

The first step is to evaluate the three performance indicators in nominal conditions over a parameter grid of $\{k_r, k_v\}$. This is represented for RT1 by the three plots of Fig. 5, where $k_r \in [3.5, 6.5]$ and $k_v \in [-3.0, -1.5]$. These plots provide a clear visualisation of the tuning trade-off mentioned before. In exactitude, a choice of gains that minimises the touchdown error (either in terms of position and velocity) will maximise the required ΔV and vice-versa.

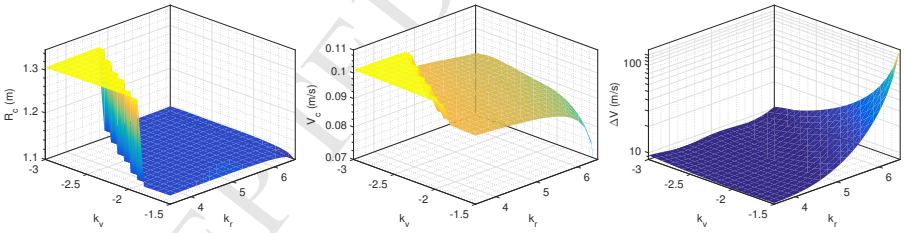

(a) Target distance (b) Closing speed (c) Total ΔV

Figure 5: Nominal performance indicators at touchdown for RT1

3.1.2. Dispersed indicators

The same principle is then employed to quantify the dispersed performance obtained with each pair $\{k_r, k_v\}$ by analysing the standard deviation of the key indicators for 100 random samples of the 19 uncertain GH coefficients in Eq. (4) with Gaussian distributions. The outcome is provided in Fig. 6, where it

is possible to observe that certain guidance solutions are associated with intense indicator peaks, which must evidently be avoided.

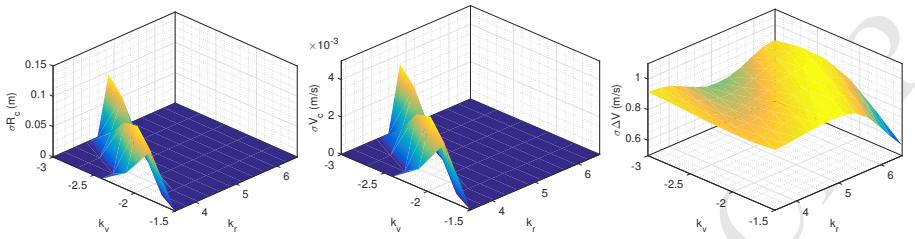

(a) Target distance (b) Closing speed (c) Total ΔV

Figure 6: Dispersed performance indicators at touchdown for RT1

3.1.3. Trade-off maps

The final step is to generate a tuning trade-off map featuring both nominal and dispersed information by overlapping the contour plots of the previous two figures. Such trade-off map is depicted in Fig. 7 for RT1.

Focusing on Fig. 7a, blue and red solid lines represent the contour plots of respectively closing speed (from Fig. 5b) and total ΔV (from Fig. 5c). Note that target distance could have been used instead of closing speed since their nominal and dispersed trends are similar. As mentioned before, a minimisation of V_c requires an increment of ΔV and vice-versa, but solutions exist such that minor degradations in V_c allow for high ΔV improvements. Furthermore, the map of ΔV has a global minimum (under 8.8 m/s), but it coincides with the area where V_c becomes significantly higher. For this reason, the transition area lies on a peak of V_c dispersion (from Fig. 6b), which is depicted in the trade-off map of Fig. 7a using dashed black lines. In the same map, the contours of ΔV dispersion (from Fig. 6c) are represented using dashed magenta lines. This plot allows to identify a global maximum (close to the standard gains {6, -2} and marked with a red $\times$) and a local minimum next to the nominal ΔV minimum.

For an easier visualisation of the observations above, Fig. 7b highlights the undesirable tuning regions of Fig. 7a. This clearly leads to the conclusion that

the standard choice of gains is not the most suitable (at least for the studied Phobos mission) since it is associated with relatively high values of both nominal and dispersed ΔV.

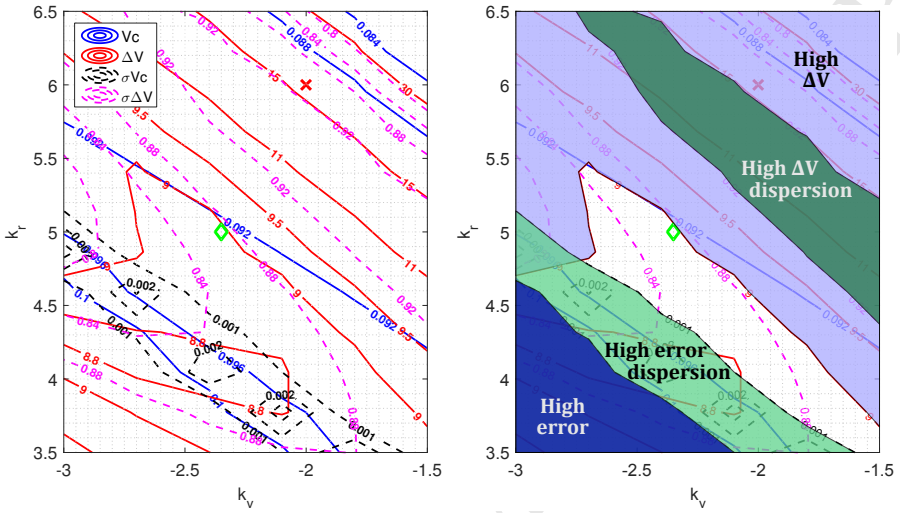

(a) Plain map (b) Map with undesirable regions

Figure 7: Guidance trade-off map for RT1 (×/◊ indicate standard/revised gains)

Hence, the proposed tuning trade-off process and maps can be systematically employed for a more favourable selection of guidance gains. For example, choosing $\{k_r, k_v\}$={5, -2.35}, marked with a green ◊ in Fig. 7a and 7b, allows ΔV to be reduced from 15.9 to less than 9 m/s while only increasing V_c from slightly more than 0.088 to approximately 0.092 m/s. At the same time, although it does not correspond to the minimum of ΔV dispersion, this choice reduces its value from around 0.9 to less than 0.88 m/s and, most importantly, keeps a safety margin with respect to the peaks of nominal and dispersed V_c.

The exact nominal values can be read directly from the map, but the dispersed indicators shall go through a more extensive Monte-Carlo (MC) validation since, for the sake of computational efficiency, the trade-off map is based on a very limited number (100) of simulations per guidance solution $\{k_r, k_v\}$.

3.2. Applicability to other trajectories

Before stepping into MC validation, however, the applicability of the tuning approach proposed in Sec. 3.1 to other D&L trajectories is assessed. Following the same procedure of the latter section, trade-off maps for RT2 and RT3, Fig. 8a and 8b, can be generated. As before, the same standard and revised choices of gains are marked with $\times$ and $\Diamond$, respectively.

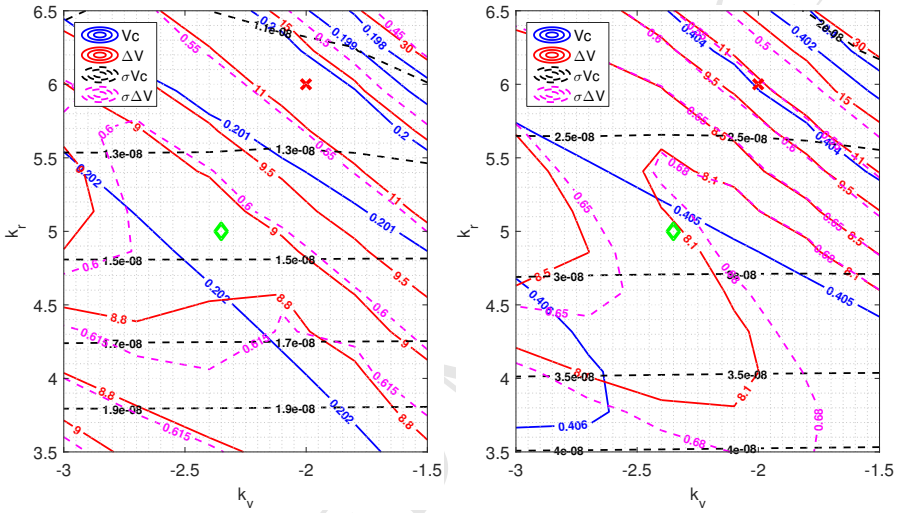

(a) RT2 (b) RT3

Figure 8: Guidance trade-off maps for other trajectories ($\times$/$\Diamond$ indicate standard/revised gains)

For both trajectories, it can be seen that, similarly to RT1, switching from standard to revised gains results in a large decrease of ΔV (about 3.5 m/s for RT2 and 2.5 m/s for RT3) with a minor increase of V_c (approximately 1 mm/s for both). The main difference between these two trajectories and RT1 is the absence of V_c dispersion peaks (dashed black lines) in the former (in which this indicator is inversely proportional to k_r). This seems to indicate the existence of a terrain hazard in RT1 where the spacecraft collides for certain guidance solutions, which is not the case in RT2 or RT3.

Also, it is possible to verify that, contrary to RT1, the revised choice of gain is not the best for RT2 and RT3 in terms of ΔV dispersion (dashed magenta lines),

since it is associated with higher values than the standard gains. However, the impact of this behaviour is much less significant than the nominal ΔV reduction and, for simplicity, the same revised gains are kept for the rest of the paper.

For a real-life application, the authors envisage the practical implementation of the proposed tuning methodology as follows:

1. High-fidelity simulation and guidance trade-off maps are generated on ground for a set of candidate D&L trajectories;
2. Once the spacecraft approaches the target and local analyses are carried out, the most suitable reference trajectory can be selected;
3. The most performing tuning selection is then determined using the appropriate trade-off map and implemented before initiating the D&L manoeuvre.

The main benefit of this approach is that guidance tuning is able to account for the actual ΔV available and acceptable landing accuracy (e.g., based on visual observations) at the time, without involving any major real-time computation.

3.3. Monte-Carlo validation

To validate the results discussed in the previous sections, the revised guidance gains $\{k_r, k_v\}$=$\{5, -2.35\}$ are now tested and compared with the standard tuning selection $\{k_r, k_v\}$=$\{6, -2\}$ using the benchmark introduced in Sec. 2.2. Each guidance tuning is simulated against the same 1000 MC samples of the 19 GH coefficients in Eq. (4) with Gaussian distributions for the three reference trajectories in Fig. 4b. As mentioned in Sec. 3.2, the revised gains have been optimised for RT1 but are kept the same for RT2 and RT3 for the sake of simplicity. Moreover, since the focus of this analysis is on the impact of the GH coefficients, no additional perturbations from actuators or navigation are included in the simulations.

The outcome of this validation campaign is depicted in Fig. 9, with a different column for each RT and using darker and lighter lines for results using respectively the standard or the revised gains. For each case, the target distance $||\mathbf{r}_f - \mathbf{r}(t)||$, closing speed $||\mathbf{v}_f - \mathbf{v}(t)||$ and required ΔV are given. Trajectories in 3D are

not shown since differences amongst them are so small that they cannot be distinguished from those in Fig. 4b.

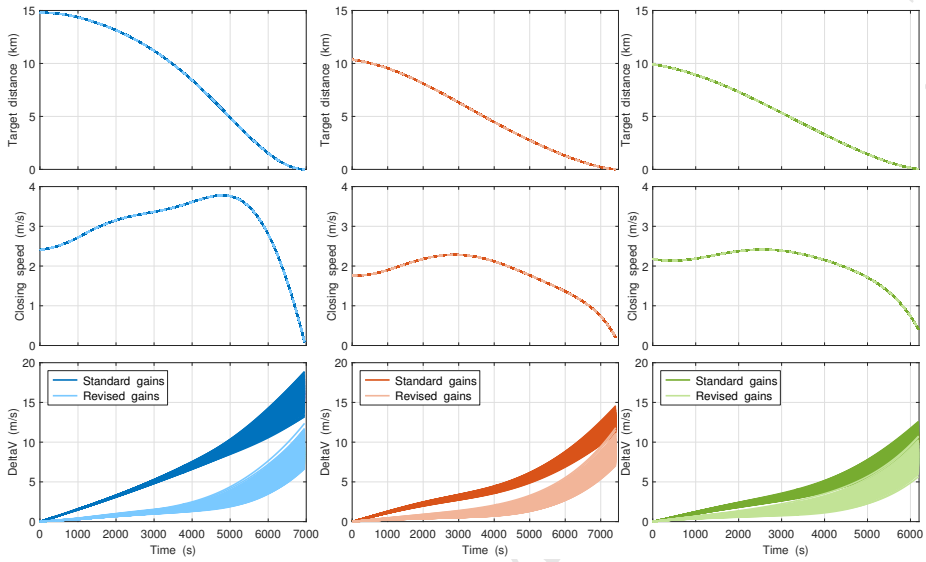

(a) RT1 (b) RT2 (c) RT3

Figure 9: High-fidelity simulation results of 1000 MC runs per trajectory with different gains

From Fig. 9 it is clear that, for the three trajectories, the revised gain selection results in significant ΔV savings with a minimal impact on position and velocity errors. Since the revised gains have been optimised for RT1, it is natural that ΔV savings are higher for this trajectory than for RT2 and RT3. For a detailed comparison, the average and standard deviation of the final values found in the MC simulations are recorded in Table 1. Note that these indicators are directly related to the ones employed for the generation of the trade-off maps in Sec. 3.1.

As anticipated from Sec. 3.1 for RT1, the revised gains enable a significant reduction in both average and dispersed ΔV at the expense of a minor increase in average and dispersed velocity error. In fact, in terms of average indicators, a ΔV reduction of 44.5% is achieved with a velocity error increase of only 3.4%. As mentioned before, these indicators can be directly read from the trade-off map of Fig. 7a. On the contrary, the dispersed indicators do not correspond

exactly to the values of Fig. 7a because the trade-off map was generated from a smaller number of simulations (100), but the mismatch is relatively small (≈9%).

Table 1: Performance comparison of 1000 MC runs per trajectory with different gains

	RT1		**RT2**		**RT3**	
Standard gains	Avg.	Std.	Avg.	Std.	Avg.	Std.
R_c (m)	1.118	8.15×10^{-5}	11.949	1.82×10^{-4}	39.053	1.72×10^{-4}
V_c (m/s)	0.089	4.91×10^{-9}	0.200	1.45×10^{-8}	0.404	2.19×10^{-8}
ΔV (m/s)	15.905	9.96×10^{-1}	12.574	6.25×10^{-1}	10.586	7.02×10^{-1}
Revised gains	Avg.	Std.	Avg.	Std.	Avg.	Std.
R_c (m)	1.117	9.80×10^{-5}	11.946	2.19×10^{-4}	39.050	2.07×10^{-4}
V_c (m/s)	0.092	6.32×10^{-9}	0.202	1.76×10^{-8}	0.405	2.64×10^{-8}
ΔV (m/s)	8.819	9.71×10^{-1}	9.009	8.00×10^{-1}	8.073	8.24×10^{-1}

Similar conclusions then hold for RT2 and RT3: the revised gains enable a significant reduction in terms of average ΔV at the expense of a minor increase in average and dispersed velocity errors as well as dispersed ΔV, as anticipated from Sec. 3.2. The latter increase is however very small (0.18 m/s for RT2 and 0.12 m/s for RT3, clearly outweighed by the average improvements of 28.5% and 23.7%, respectively) and could have been compensated by a dedicated choice of guidance gains for each trajectory.

With the aforementioned observations in mind, not only does this section validate the proposed guidance tuning methodology, it also confirms that the state-of-practice tuning selection, based on the cost function of Eq. (10) and on the assumption of simplified and well-known gravitational fields, is not fuel-optimal for the case of Phobos.

4. Reconciliation with structured $\mathcal{H}_\infty$ optimisation

This section shows how the guidance tuning methodology proposed in Sec. 3 can reconcile and complement alternative approaches such as the structured $\mathcal{H}_\infty$ optimisation, which is able to explicitly account for uncertainties. The specific

interest on structured $\mathcal{H}_\infty$ is further motivated in Sec. 4.1 and the uncertainty modelling process is summarised in Sec. 4.2. The application of structured optimisation to guidance tuning is detailed in Sec. 4.3 and comparative results are provided in Sec. 4.4.

4.1. Why structured $\mathcal{H}_\infty$ optimisation?

The closed-loop guidance laws addressed in this paper, see Eq. (9), have a fixed structure parameterised by tuneable gains $\{k_r,\ k_v\}$, which makes them perfect candidates for the application of the novel structured $\mathcal{H}_\infty$ optimisation paradigm. The capability of this paradigm in taking advantage of state-of-practice guidance structures and industry legacy knowledge is a very important point as it enables the transfer of the tuning approach to industry without representing a disruptive change in the design teams.

In addition to this capability, the application of structured $\mathcal{H}_\infty$ optimisation to the D&L problem offers two other main advantages:

- As it is founded on Robust Control (Apkarian et al., 2015) it allows to explicitly account for uncertain gravitational environments;
- It is able to handle directly and simultaneously multiple tuning goals and design models (Gahinet & Apkarian, 2011) thus providing solutions that are guaranteed for a set of operating points in space or reference trajectories.

Naturally, these advantages come at the expense of a challenging (non-smooth) mathematical problem and, to solve it, structured $\mathcal{H}_\infty$ employs local optimisation methods. To mitigate the local nature of the optimiser, multiple runs are often performed from random starting points. This represents a key issue within the Space industry due to certification concerns and also a breakdown in the design learning experience (i.e., the assessment of system behaviour changes due to changes in the posing of the problem).

Despite this challenge, the strengths mentioned above make structured $\mathcal{H}_\infty$ a very industry-oriented approach and its effectiveness has already been proven through two Space-flown missions (Falcoz et al., 2015; Pittet & Prieur, 2015) and

more recently in piloted flight tests (Marcos & Sato, 2017). Under the scope of planetary D&L, the application presented in (Falcoz et al., 2015) is particularly interesting since it showed that structured $\mathcal{H}_\infty$ could be employed successfully for the refinement of the European Rosetta's orbit controller after thruster authority degradation. The revised gains were uploaded to the spacecraft just before its braking and final insertion manoeuvres with the target comet in May 2014.

The structured $\mathcal{H}_\infty$ algorithm is part of the `hinfstruct` and `systune` routines of MATLAB, with the latter including an easier quantification of $\mathcal{H}_\infty$ objectives and handling of multiple control requirements, channels and models. A detailed description of guidance tuning via structured $\mathcal{H}_\infty$ optimisation is provided in Sec. 4.3, followed by the reconciliation of results in Sec. 4.4. Before that, Sec. 4.2 introduces how the two features stated above (i.e., ability to account for uncertainties and for multiple points in space) are included within this tuning approach.

4.2. Gravitational uncertainty modelling

The development of models that allow to capture gravitational uncertainty effects is based on the so-called linearised orbital perturbation theory (Battin, 1987). According to this theory, state and control variables can be defined at different operating points along a given trajectory as the sum of a reference (desired) value and small perturbations (deviations). The dynamics of these perturbations is then approximated by the 1$^{\text{st}}$ order terms of the Taylor series expansion of $\mathbf{f}\left(\mathbf{r}(t), \mathbf{v}(t), \nu(t)\right)$ from Eq. (5) around the reference points:

$$\begin{bmatrix} \delta\dot{\mathbf{r}}(t) \\ \delta\dot{\mathbf{v}}(t) \\ \delta\dot{\nu}(t) \end{bmatrix} = J_{\mathbf{f}}(t) \begin{bmatrix} \delta\mathbf{r}(t) \\ \delta\mathbf{v}(t) \\ \delta\nu(t) \end{bmatrix} + \begin{bmatrix} 0_{3\times3} \\ I_{3\times3} \\ 0_{1\times3} \end{bmatrix} \delta\mathbf{a}(t) \tag{11}$$

where the Jacobian matrix is given by:

$$J_{\mathbf{f}}(t) = \left[\frac{\partial\mathbf{f}}{\partial\mathbf{r}} \quad \frac{\partial\mathbf{f}}{\partial\mathbf{v}} \quad \frac{\partial\mathbf{f}}{\partial\nu} \right] \Bigg|_{\substack{\mathbf{r}=\mathbf{r}_{\text{ref}}(t) \\ \mathbf{v}=\mathbf{v}_{\text{ref}}(t) \\ \nu=\nu_{\text{ref}}(t)}} \tag{12}$$

and computed via finite differences due to the complexity of $\mathbf{f}\left(\mathbf{r}(t), \mathbf{v}(t), \nu(t)\right)$. Performing this linearisation at different instants of time t_i, $i = \{1, \ldots, N\}$ along a reference trajectory allows to generate a set of linear time-invariant (LTI) "spacecraft dynamics & kinematics" (SDK) models $G^i_{\mathrm{SDK}}(\mathrm{s})$, with the following state-space description:

$$\left[\begin{array}{c} \dot{\mathbf{x}}_{\mathrm{SDK}}(\mathrm{s}) \\ \hline \delta\mathbf{r}(\mathrm{s}) \\ \delta\mathbf{v}(\mathrm{s}) \end{array}\right] = \left[\begin{array}{cc|c} & & 0_{3\times3} \\ & J^i_{\mathbf{f}} & I_{3\times3} \\ & & 0_{1\times3} \\ \hline I_{6\times6} & 0_{6\times1} & 0_{6\times3} \end{array}\right] \left[\begin{array}{c} \mathbf{x}_{\mathrm{SDK}}(\mathrm{s}) \\ \hline \delta\mathbf{a}(\mathrm{s}) \end{array}\right] \tag{13}$$

where $J^i_{\mathbf{f}} = J_{\mathbf{f}}(t_i)$ and $\mathbf{x}_{\mathrm{SDK}}(\mathrm{s})$ is the internal state vector.

As introduced in Sec. 2.1, 19 out of the 28 GH coefficients are highly inaccurately known. This means that the computation of $J^i_{\mathbf{f}}$ and thus the description of $G^i_{\mathrm{SDK}}(\mathrm{s})$ in Eq. (13) is subject to a high level of uncertainty. To capture the effect of this uncertainty, a mathematical representation known as linear fractional transformation (LFT) is employed (Doyle et al., 1991; Zhou et al., 1995). LFTs are particularly attractive due to their extreme modularity and because typical algebraic operations preserve the LFT structure. Therefore, in an interconnected system, it is common to isolate what is known as an LTI system and gather all the "troublemaking" (uncertain, time-varying or nonlinear) components into an operator Δ with normalised infinity norm, $||\Delta||_\infty \leq 1$.

Representative LFT models of $G^i_{\mathrm{SDK}}(\mathrm{s})$ have been built through a modelling procedure that relies on the interpolation of dispersed samples of $J^i_{\mathbf{f}}$. Details on this process can be encountered in (Simplício et al., 2018). In the end, a set of $N = 10$ models has been generated, covering 10 design points with uniform closing speed intervals.

4.3. Application of structured $\mathcal{H}_\infty$ optimisation to guidance tuning

The main difficulty in the application of structured $\mathcal{H}_\infty$ optimisation to the D&L problem lies on its formulation as an $\mathcal{H}_\infty$ problem. As introduced in Sec. 2.2.2, state-of-practice guidance solutions have been found by recasting

it as an optimal control problem with the cost function given in Eq. (10) and constrained terminal position and velocity. This is substantially different from the structured $\mathcal{H}_\infty$ problem, which aims at minimising the induced $\mathcal{H}_\infty$-norm of pre-specified input-output control channels:

$$\min_{k_r,\, k_v} \; \{\max\left(||M_1(\mathrm{s})||_\infty, \ldots, ||M_N(\mathrm{s})||_\infty\right)\} \tag{14}$$

where $M_i(\mathrm{s})$, with $i = \{1, \ldots, N\}$, are linear representations of the system dynamics at different operating points along one or more reference trajectories.

All the necessary system interconnections have been implemented in Simulink and the models $M_i(\mathrm{s})$ have been retrieved using its `slTuner` interface, which allows to automatically create linear models of Simulink systems featuring tuneable parameters (in this case $\{k_r,\ k_v\}$). The Simulink block diagram employed for guidance tuning is depicted in Fig. 10.

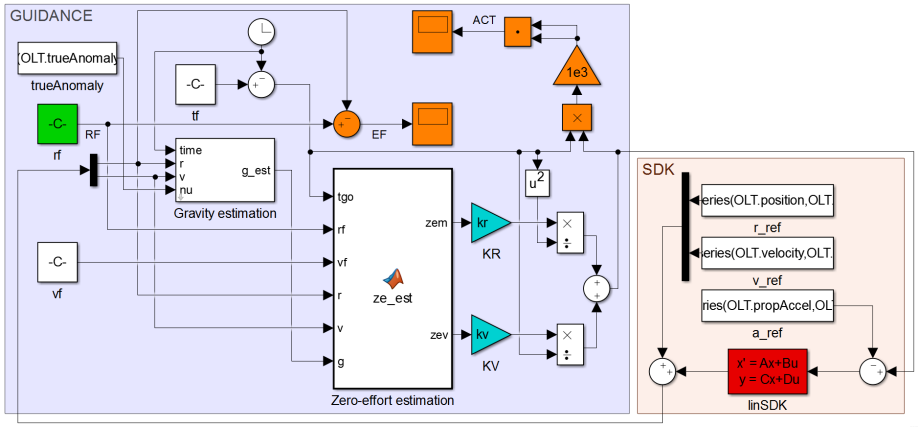

Figure 10: Simulink model for structured guidance tuning

The linear representations $M_i(\mathrm{s})$ include not only the SDK dynamics, but also the structure of the guidance algorithm involved. Furthermore, the SDK dynamics can be conveniently replaced by the orbital perturbation model of Eq. (13) to consider a multi-plant design, adding in this case the required information to convert between total and perturbed variables. The guidance algorithm block includes, in addition to the parameterised structure (i.e. the

gains $\{k_r,\, k_v\}$), estimators for the apparent gravity (Eq. (6)), zero-effort miss (Eq. (1)) and velocity (Eq. (2)).

Furthermore, the Simulink model highlights (with green-orange blocks) input-output control channels, which provide the basis for the definition of tuning objectives. Objective specification is a key factor, often resulting from a highly iterative process. The process followed in this article is illustrated in Fig. 11 and described in the following paragraphs.

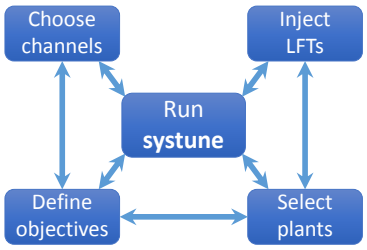

Figure 11: Structured guidance tuning process

The first step in this process is the selection of input and output channels with respect to which the tuning objectives will be defined. The channels must contain the gains $\{k_r,\, k_v\}$ on their path and be physically related to the intended tuning objectives. Following the same reasoning of Sec. 3.1, two competing goals are addressed: *accuracy* (minimising touchdown error) and *efficiency* (minimising propellant consumption). To do so, the touchdown position vector $\mathbf{r}_f$ is selected as control input and two dedicated output signals are defined:

- $\mathbf{z}_r(t) = \mathbf{r}_f - \mathbf{r}(t)$, measuring the deviation with respect to touchdown site. **Remark:** a velocity deviation could have also been included, but it was found to be redundant and hence not considered for the sake of simplicity.
- $z_a(t) = \mathbf{a}^{\mathrm{T}}(t)\,\mathbf{a}(t)\left(\dfrac{t_{\mathrm{go}}(t)}{10^{-3}}\right)^2$, quantifying the instantaneous actuation effort commanded to compensate for the former deviation. **Remark:** the acceleration signal is scaled by $t_{\mathrm{go}}(t)$ to normalise this indicator throughout

the descent (recall that actuation effort tends to increase as $t_{\text{go}}(t) \to 0$) and by a constant factor of 10^3 to operate with more suitable units (mm/s^2 instead of m/s^2).

As mentioned above, the choice of channels is not deterministic and may have to be revisited depending on the outcome of the optimisation or if the tuning objectives change. In this article, objectives are defined by constraining the $\mathcal{H}_\infty$-norm of the control channels (which physically represents the worst-case amplification of energy-bounded inputs) as follows:

$$\begin{cases} ||M_{\mathbf{r}_f \to \mathbf{z}_r}(\text{s})||_\infty < \dfrac{\gamma_{\text{acc}}}{\alpha} \\ ||M_{\mathbf{r}_f \to z_a}(\text{s})||_\infty < \dfrac{\gamma_{\text{eff}}}{\alpha - 1} \end{cases} \tag{15}$$

In this equation, $M_{\mathbf{r}_f \to \mathbf{z}_r}(\text{s})$ and $M_{\mathbf{r}_f \to z_a}(\text{s})$ are the control channel transfer functions (obtained with `slTuner`) which depend on $\{k_r, k_v\}$, and the parameters $\gamma_{\text{acc}} > 0$ and $\gamma_{\text{eff}} > 0$ represent the constraints associated with *accuracy* and *efficiency* goals. The constant $\alpha \in]0, 1[$ is a parameter that allows to exploit the underlying trade-off between the two goals (when $\alpha \to 1$ the optimiser focuses on *accuracy* only and vice-versa). The interval is open in order to prevent the singularity in Eq. (15). γ_{acc} and γ_{eff} can be frequency-dependent but, for simplicity, constant values of 0.16 and 25, respectively, have been adopted. Once again, these values have been chosen iteratively and may need revisiting based on the models used for the optimisation.

Selecting the linear models to be considered is in fact another key step in the process. Different design plants $M_i(\text{s})$ can be specified through the `findop` function, which runs the Simulink model up to the desired operating point and provides the linear representation at that point. Following the multi-plant approach of Eq. (14), plants $M_i(\text{s})$ are then aggregated in a block-diagonal structure. In this article, all the design models have been considered except the last one ($i = 10$ and $t = t_f$) as it leads to $t_{\text{go}} = 0$. This choice is also affected by how tight performance requirements and robustness specifications are.

Finally, robustness against gravitational uncertainties can be explicitly accounted for by replacing the LTI SDK models in Fig. 10 by the LFTs of Sec. 4.2.

The LFTs can be easily injected via the `BlockSubs` field of `slTuner`. At each step of the iterative process in Fig. 11, the `systune` routine is then called to find optimal gains $\{k_r, k_v\}$ that meet the requirements of Eq. (15) at every chosen operating point under nominal or dispersed gravitational conditions.

4.4. Comparison of results

The guidance tuning results obtained for RT1 using the setup described in the previous section are depicted in Fig. 12, which shows the optimal gains $\{k_r, k_v\}$ for different values of $\alpha \in]0, 1[$ (and therefore different objective combinations of *efficiency* and *accuracy*). Continuous lines represent the nominal (NOM) solution and dashed lines that derived using the LFT models. For the optimisation, the two gains are initialised with their state-of-practice values {6, -2} and allowed to vary within the same intervals considered in Sec. 3.1. These values are also indicated in the figure by thin horizontal, black lines.

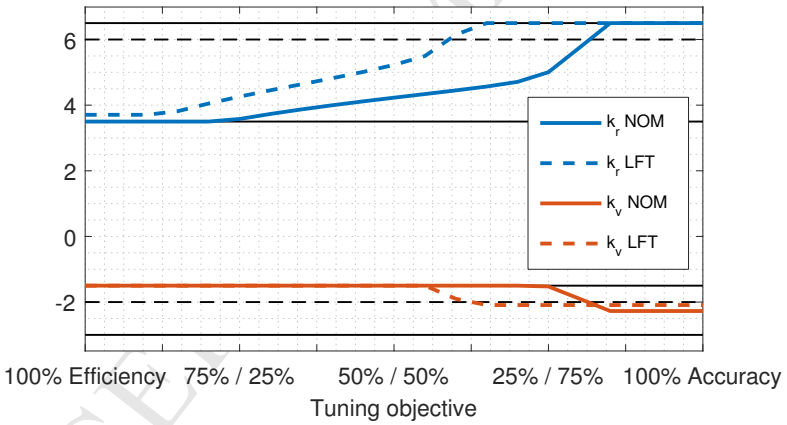

Figure 12: Guidance tuning trade-off results for RT1

From this figure, it is clear that extreme tuning objectives (100% *efficiency* or 100% *accuracy*) lead to a completely opposite trend in optimal gains. This trade-off was already anticipated based on the understanding provided by the trade-off maps. Note also that, for 100% *accuracy*, the optimal value of k_v would reach its lower limit if k_r was allowed to have higher values.

Between the two extremes, there is a smooth transition of optimal gains as a function of the objective combination. This transition is different for the nominal and LFT solutions. For a clearer interpretation of results, the structured $\mathcal{H}_\infty$ tuning (stune) solutions of Fig. 12 are plotted in cyan over the trade-off map of RT1 (from Fig. 7) in Fig. 13. Intermediate trade-off points are also highlighted.

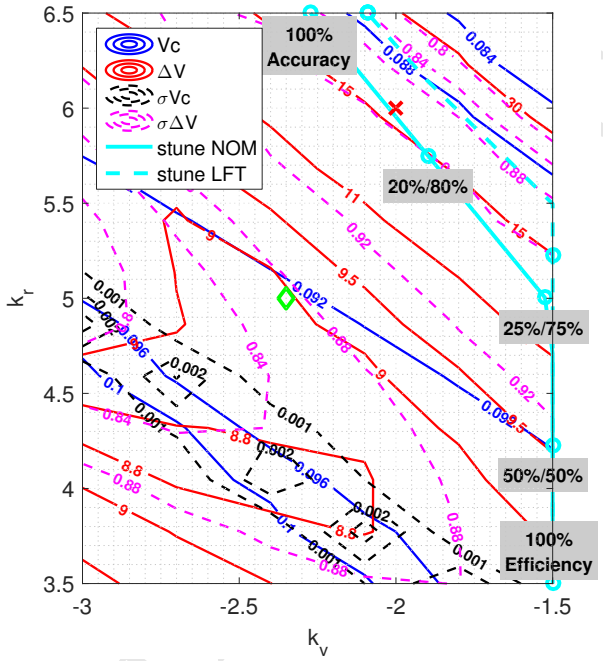

Figure 13: Visualisation of tuning results over the trade-off map of RT1

From here, it is confirmed that the difference between optimal nominal and LFT results is consistent with the understanding provided by the trade-off map, that is, LFT solutions are shifted towards the top right corner of the plot, away from the dispersion peaks of both touchdown error and total ΔV.

The main observation, however, is that, using the structured $\mathcal{H}_\infty$ guidance tuning methodology, the standard gain selection of {6, -2} (given by the red $\times$) could be successfully recovered. This takes place for nominal conditions, the same under which the gains were analytically derived, and for a combination of 83% *accuracy* / 17% *efficiency*. The fact that the ratio between *accuracy* and

efficiency requirements is so high in this case is again related to the way the D&L control problem (Sec. 2.2.2) was formulated: since terminal position and velocity are constrained variables in this problem, it is reasonable that *accuracy* goals have a stronger impact in the $\mathcal{H}_\infty$-norm trade-off.

Nevertheless, for this scenario, the structured tuning approach was unable to capture more performing guidance solutions (e.g. the one marked with the green $\Diamond$), such as that obtained using the trade-off maps and systematic methodology proposed before. This is due to the loss of highly nonlinear effects with the linearisations performed by `slTuner`, as well as of their propagation throughout the D&L trajectory. It represents the main limitation of the method (endemic to all LTI-based design and tuning approaches) and is a topic currently under investigation.

5. Conclusions

This paper proposes a systematic tuning methodology for closed-loop Space descent & landing (D&L) guidance laws. The proposed methodology employs a systematic evaluation of high-fidelity models to generate trade-off maps that provide clear performance and robustness quantifications of candidate solutions.

The ability to account for nonlinear and uncertain dynamics is a key aspect of this methodology, which is particularly important when targeting planetary bodies with complex and uncertain environments. In fact, it is shown that, for a landing on Phobos, propellant consumption savings of around 40% could be achieved (for similar errors) compared to state-of-practice tuning selections derived under the assumption of simplified and well-known gravitational fields.

In addition, trade-off maps can be generated before the D&L mission but only applied once the spacecraft approaches the target body, having in consideration the actual propellant available and without the need for expensive computations, which makes this approach very industry-oriented. Also with this in mind, the applicability of structured $\mathcal{H}_\infty$ optimisation has also been addressed as a way to exploit the fixed structure of D&L guidance laws.

Comparative results are presented in this paper regarding the reconciliation and complementarity of the two tuning processes, but research on this topic is still ongoing. This is mostly related to the fact that, although the state-of-practice tuning selections could be recovered by the structured $\mathcal{H}_\infty$ approach, superior guidance solutions, identified with trade-off maps, could not be captured due to the propagation of highly nonlinear dynamics inherent to the problem.

References

Apkarian, P., Dao, M., & Noll, D. (2015). Parametric robust structured control design. *Transactions on Automatic Control*, *60*, 1857–1869.

Barraclough, S., Ratcliffe, A., Buchwald, R., Chapuy, M., Garland, M., & Rebuffat, D. (2014). Phootprint: A European Phobos Sample Return Mission. In *The 11th International Planetary Probe Workshop*. Passadena, CA.

Battin, R. (1987). *An Introduction to the Mathematics and Methods of Astrodynamics*. (1st ed.). AIAA Education Series.

Bhaskaran, S., Mastrodemos, N., Riedel, J., & Synnott, S. (2004). Optical Navigation for the STARDUST Wild 2 Encounter. In *The 18th International Symposium on Space Flight Dynamics*. Munich, Germany.

Doyle, J., Packard, A., & Zhou, K. (1991). Review of LFTs, LMIs and μ. In *The 30th IEEE Conference on Decision and Control*. Brighton, UK.

D'Souza, C. (1997). An optimal guidance law for planetary landing. In *The 1997 AIAA Guidance, Navigation, and Control Conference*. New Orleans, LA.

Ebrahimi, B., Bahrami, M., & Roshanian, J. (2008). Optimal sliding-mode guidance with terminal velocity constraint for fixed-interval propulsive maneuvers. *Acta Astronautica*, *62*, 556–562.

Falcoz, A., Pittet, C., Bennani, S., Guignard, A., Bayart, C., & Frapard, B. (2015). Systematic design methods of robust and structured controllers for satellites. *Space Journal*, *7*, 319–334.

Ferrari, F., Lavagna, M., Scheper, M., Burmann, B., & Carnelli, I. (2015). The European Asteroid Impact Mission: Phase A Design and Mission Analysis. In *The 2015 AAS/AIAA Astrodynamics Specialist Conference*. Vail, CO.

Gahinet, P., & Apkarian, P. (2011). Structured $\mathcal{H}_\infty$ Synthesis in MATLAB. In *The 18th IFAC World Congress*. Milan, Italy.

Geurts, K., Fantinati, C., Ulamec, S., & Willnecker, R. (2014). Rosetta Lander: On-Comet Operations Preparation and Planning. In *The AIAA SpaceOps 2014 Conference*. Passadena, CA.

Gil-Fernandez, J., Panzeca, R., & Corral, C. (2008). Impacting Small Near Earth Objects. *Advances in Space Research*, *42*, 1352–1363.

Guo, Y., Hawkins, M., & Wie, B. (2011). Optimal Feedback Guidance Algorithms for Planetary Landing and Asteroid Intercept. In *The 2011 AAS/AIAA Astrodynamics Specialist Conference*. Girdwood, AK.

Hawkins, M., Guo, Y., & Wie, B. (2012). Spacecraft Guidance Algorithms for Asteroid Intercept and Rendezvous Missions. *International Journal of Aeronautical and Space Sciences*, *13*, 154–169.

Joffre, E., Zamaro, M., Silva, N., Marcos, A., Simplício, P., & Richardson, B. (2017). Landing on Small Bodies Trajectory Design, Robust Nonlinear Guidance and Control. In *The 27th AAS/AIAA Spacefilght Mechanics Meeting*. San Antonio, TX.

Kubitschek, D. (2003). Impactor spacecraft targeting for the Deep Impact mission to comet Temple 1. In *The 2003 AAS/AIAA Astrodynamics Specialist Conference*. Big Sky, MT.

Lauretta, D., & OSIRIS-REx Team (2012). An Overview of the OSIRIS-REx Asteroid Sample Return Mission. In *The 43rd Lunar and Planetary Science Conference*. Woodlands, TX.

Marcos, A., & Sato, M. (2017). Flight Testing of a Structured H-infinity Controller: a EU-Japan Collaborative Experience. In *The 1st IEEE Conference on Control Technology and Applications*. Kohala Coast, HI.

Pittet, C., & Prieur, P. (2015). Structured accelero-stellar estimator for MICROSCOPE drag-free mission. In *The 3rd CEAS EuroGNC Conference*. Toulouse, France.

Simplício, P., Marcos, A., Joffre, E., Zamaro, M., & Silva, N. (2017). Parameterised Laws for Robust Guidance and Control of Planetary Landers. In *The 4th CEAS EuroGNC Conference*. Warsaw, Poland.

Simplício, P., Marcos, A., Joffre, E., Zamaro, M., & Silva, N. (2018). Synthesis and analysis of robust control compensators for Space descent & landing. *International Journal of Robust and Nonlinear Control*, *Article in Advance*.

Yoshimitsu, T., Kawaguchi, J., Hashimoto, T., Kubota, T., Uo, M., Morita, H., & Shirakawa, K. (2009). Hayabusa – final autonomous descent and landing based on target marker tracking. *Acta Astronautica*, *65*, 657–665.

Zamaro, M., & Biggs, J. (2015). Natural motion around the Martian moon Phobos: the dynamical substitutes of the Libration Point Orbits in an elliptic three-body problem with gravity harmonics. *Celestial Mechanics and Dynamical Astronomy*, *122*, 263–302.

Zarchan, P. (1994). *Tactical and Strategic Missile Guidance*. (2nd ed.). AIAA Progress in Astronautics and Aeronautics.

Zhou, K., Doyle, J., & Glover, K. (1995). *Robust and Optimal Control*. (1st ed.). Prentice-Hall.